Catalyzed Ethanol Chemical Looping Gasification Mechanism on the Perfect and Reduced Fe$_2$O$_3$ Surfaces

Laixing Luo [1], Xing Zheng [1], Jianye Wang [2], Wu Qin [1], Xianbin Xiao [1,*] and Zongming Zheng [1]

[1] National Engineering Laboratory for Biomass Power Generation Equipment, School of New Energy, North China Electric Power University, Beijing 102206, China; 13120148195@163.com (L.L.); zhengxing3375@163.com (X.Z.); qinwu@ncepu.edu.cn (W.Q.); zmzheng@vip.126.com (Z.Z.)

[2] State Key Laboratory of Alternate Electrical Power System with Renewable Energy Sources, North China Electric Power University, Beijing 102206, China; wjyncepu@163.com

* Correspondence: xiaoxianbin@ncepu.edu.cn

Abstract: Biomass chemical looping gasification (CLG) is a novel gasification technology for hydrogen production, where the oxygen carrier (OC) transfers lattice oxygen to catalytically oxidize fuel into syngas. However, the OC is gradually reduced, showing different reaction activities in the CLG process. Fully understanding the CLG reaction mechanism of fuel molecules on perfect and reduced OC surfaces is necessary, for which the CLG of ethanol using Fe$_2$O$_3$ as the OC was introduced as the probe reaction to perform density functional theory calculations to reveal the decomposition mechanism of ethanol into the synthesis gas (including H$_2$, CH$_4$, ethylene, formaldehyde, acetaldehyde, and CO) on perfect and reduced Fe$_2$O$_3$(001) surfaces. When Fe$_2$O$_3$(001) is reduced to FeO$_{0.375}$(001), the calculated barrier energy decreases and then increases again, suggesting that the reduction state around FeO(001) favors the catalytic decomposition of ethanol to produce hydrogen, which proves that the degree of reduction has an important effect on the CLG reaction.

Keywords: gasification; adsorption; biomass; oxygen carrier; DFT

1. Introduction

Realizing the aggregate fossil fuel demand peak and achieving 1.5 °C Pathway of Paris Agreement goals require the acquisition of more new and renewable energy in the global energy mix. As a clean, renewable, zero-emission energy, hydrogen is a promising energy carrier to diversify the energy supply and promote the energy consumption transition. Although hydrogen is the most common element in the universe, natural hydrogen occurs not in an elemental form but in hydrogen-containing compounds. The chemical looping gasification (CLG) approach to hydrogen production has received widespread attention due to its high efficiency and low carbon emissions. Unlike traditional gasification technology with molecular oxygen as the gasification agent, CLG uses lattice oxygen in the oxygen carrier (OC) to produce syngas [1,2]. A schematic diagram of the CLG is shown in Figure 1. CLG technology consists of two interconnected reactors, and the OC transfers lattice oxygen and heat in the reactor. The OC is reduced by fuel feedstock in the fuel reactor (FR) and is oxidized by the high temperature in the air reactor (AR) alternately. The fuel and syngas are inherently separated from air and nitrogen. The fuel gas is subjected to subsequent condensation to remove moisture. The resulting higher concentration of CO$_2$ could be obtained with low energy consumption [3,4].
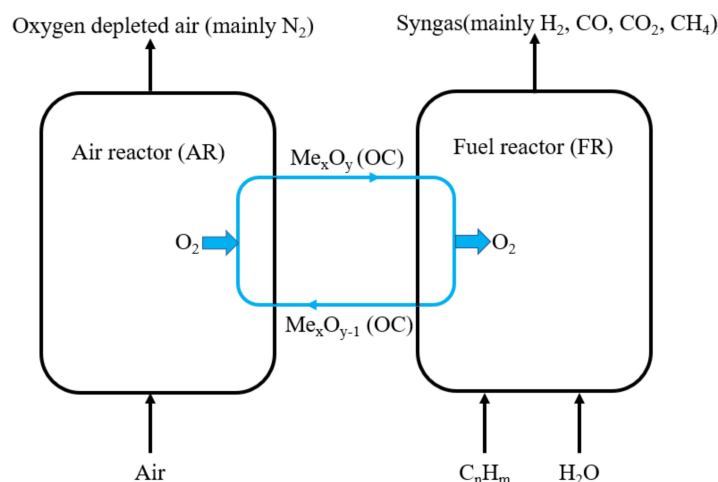
Figure 1. Schematic diagram of the chemical looping gasification (CLG) system.

The OC plays a key role in the CLG process, which is not only an oxygen carrier but also a heat carrier. A competent OC should have the following characteristics [4–6]: high reactivity and oxygen transfer performance, stable chemical and thermodynamic properties, a low price, good environmental friendliness, good sintering resistance, good mechanical strength, and wear resistance. Common OCs used in CLG include nickel-based OCs [7], copper-based OCs, manganese-based OCs, cobalt-based OCs, and iron-based OCs [8,9]. In recent years, iron-based OCs have been thoroughly investigated due to their environmental friendliness, nontoxicity, harmlessness, and low cost [10–12]. Huang et al. [13] used iron ore as an OC to study the effects of the oxygen excess number, steam concentration, oxygen source, and cycle times on CLG. Zeng et al. [5,14] used a double-fluidized bed gasifier to conduct CLG experiments of biomass such as sawdust based on iron-based OC. Wei et al. [15] assessed the behavior of an iron–nickel composite OC in a 10 kW CLG unit. In addition, the research results show that iron-based OCs not only effectively transfer oxygen and heat but also have an effect on the catalytic gasification of tar and coke macromolecules, which improves the fuel conversion efficiency. It is found that the multiphase OC complex can improve the specific surface area and promote the delivery of lattice oxygen from the theoretical calculations based on the density functional theory [16–18]. However, the solid CLG process still has an insufficient gasification agent, an insufficient solid–solid interaction, and a low carbon conversion rate. In previous work, our team employed simultaneous chemical looping combustion with solid fuel and organic waste liquid. During the degradation of the organic waste liquid, high-temperature water vapor was produced to provide the gasification agent and promote solid fuel gasification [16–21]. Dou et al. [22] used nickel-based OC to produce hydrogen in ethanol–steam CLG and explained the decomposition mechanism of ethanol on the nickel-based OC. However, the decomposition mechanism of ethanol on iron-based OCs of different reduction degrees is still rarely reported, and the underlying mechanism of the CLG process is still unclear. The catalysis behavior on the surface of the OC needs to be clarified in detail.

In this paper, the density functional theory calculation method is used to study the adsorption characteristics and decomposition reaction path of ethanol on fully reduced $Fe_2O_3(001)$, which reveals the formation mechanism of the synthesis gas products such as H_2, CH_4, ethylene, formaldehyde, acetaldehyde, and CO in the ethanol chemical looping reforming experiment. Studying the gradual reduction process of the OC and the interaction mechanism between liquid or solid fuel and the surface of the OC can accumulate basic kinetic and thermodynamic parameters for the chemical looping reaction system of substances. This is conducive to the development and engineering application of chemical looping technology.

2. Materials and Methods

The Fe_2O_3 unit cell is a rhombohedral R-3c space group structure containing 6 iron atoms and 4 oxygen atoms. The Fe_2O_3(001) surface is one of the most stable crystal planes exposed in natural iron ore [23,24]. The Fe_2O_3 model was imported from the structure file in the Materials Studio (MS) software package. A 5 atomic layer 2×2 Fe_2O_3 (001) surface was constructed along the direction of the crystal plane of Fe_2O_3(001), with a 1.2 nm vacuum gap to avoid interaction between surfaces. Oxygen atoms were gradually removed from the surface of the 2×2 Fe_2O_3(001) to simulate the reduced Fe_2O_3(001) surface, including Fe_3O_4(001), FeO(001), and $FeO_{0.375}$(001). Through geometric optimization, the stable surface configuration is shown in Figure 2. On a stable surface, with the adsorption and decomposition reactions of ethanol molecules, all calculations were based on dispersion-corrected density function theory (DFT-D) [25]. The electronic exchange-related energy was described by the Perdew-Burke-Ernzerhof (PBE) exchange-correlation function [26,27] and the generalized gradient approximation [12,28], and the ion core was described by the supersoft pseudopotential [29]. Taking into account the strong spin polarization effect, the antiferromagnetic arrangement of Fe atoms in the Fe_2O_3 unit cell was set to +−+; +, referring to the upward and downward rotation directions relative to the *z*-axis to achieve the total energy of the smallest stable state model [30]. In the calculation process, all atoms were allowed to relax, the truncation energy was set to 350 eV, the tail width was 0.1 eV, and the K point density was $4 \times 4 \times 1$. In a self-consistent field, the convergence criteria for energy, maximum force, maximum stress, and displacement were 2.0×10^{-5} eV/atom, 0.002 Ha/Å, 0.1 GPa, and 0.002 Å, respectively. The transition state search adopted the linear/secondary synchronous transition method (LST/QST) [31]. All calculations were performed using the CASTEP code in the MS software package.
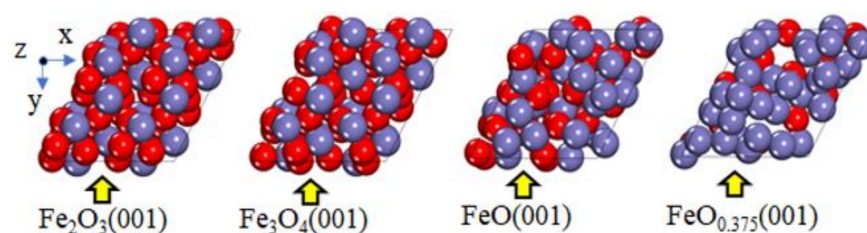

Figure 2. Stable $2 \times 2Fe_2O_3$(001), Fe_3O_4(001), FeO(001), and $FeO_{0.375}$(001) (⬤O and ⬤Fe).

3. Results and Discussion

3.1. Adsorption of Ethanol on the Perfect and Reduced Fe_2O_3(001)

The stable configuration of ethanol adsorption on the ideal and reduced Fe_2O_3 surface is shown in Figure 3. The adsorption of ethanol molecules on each surface is physical adsorption. The adsorption position and direction of ethanol on each surface are different. With the increase of the OC reduction degree, the bond length of the Fe-O bond and Fe-Fe bond increases, and the pores of the surface model increase as well.
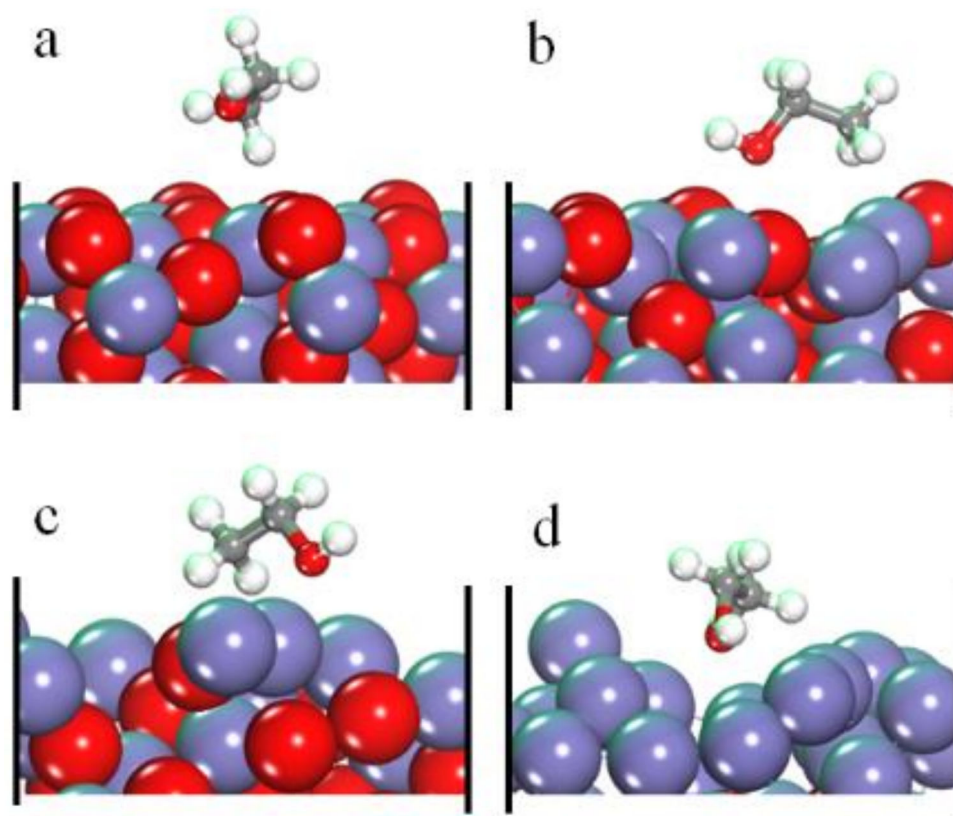
Figure 3. Stable configurations of ethanol adsorption on the (**a**) $Fe_2O_3(001)$, (**b**) $Fe_3O_4(001)$, (**c**) FeO(001), and (**d**) $FeO_{0.375}(001)$ surfaces (⬤O, ⬤Fe, ⬤H, and ⬤C).

The surface interaction between ethanol and $Fe_2O_3(001)$, $Fe_3O_4(001)$, FeO(001), and $FeO_{0.375}(001)$ can be characterized by adsorption energy (E_{ads}). E_{ads} is calculated by the following formula:

$$E_{ads} = E_{AB} - E_A - E_B \tag{1}$$

Among them, E_{AB} represents the total energy of the model system after adsorption, E_A represents the energy of the OC ($Fe_2O_3(001)$, $Fe_3O_4(001)$, FeO(001), and $FeO_{0.375}(001)$), and E_B represents the energy of the adsorbate. E_{AB}, E_A, and E_B can be obtained from "final energy" in the optimized model file. As shown in Figure 4, the adsorption energy of ethanol molecules on each surface is negative, which indicates the adsorption process can achieve stability by releasing heat.
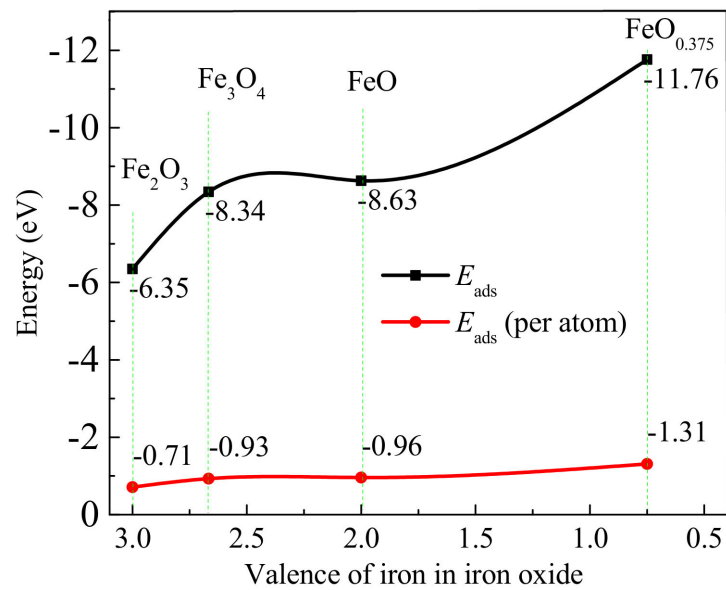
Figure 4. Adsorption energy for ethanol adsorption on $Fe_2O_3(001)$, $Fe_3O_4(001)$, $FeO(001)$, and $FeO_{0.375}(001)$.

The bond length of the ethanol molecule of each adsorption system is shown in Table 1. With the increase in the degree of OC reduction, the bond length of the C1-H bond on the ethanol molecule does not change much, and the bond length is about 1.1 Å. The C2-H bond length gradually decreases, which may be caused by the continuous increase in the C-OH bond length of the hydroxyl bond connected to the C2 atom. The O-H bond length gradually increases. The increase in the bond length of the C-OH bond and O-H bond may be caused by the interaction of the OC surface with ethanol, which provides the necessary conditions for the dehydroxylation of hydrogen atoms of ethanol molecules.

Table 1. Bond length parameters of the adsorbed ethanol molecule on each surface.

Different Reduction Surfaces of Iron Oxide	C1-H(Å)	C2-H(Å)	C-C(Å)	C-O(Å)	O-H(Å)
			Bond Length		
$Fe_2O_3(001)$	1.101	1.107	1.520	1.442	0.974
$Fe_3O_4(001)$	1.099	1.106	1.516	1.454	0.975
$FeO(001)$	1.097	1.105	1.505	1.477	0.975
$FeO_{0.375}(001)$	1.101	1.104	1.514	1.481	0.983

C1: methyl carbon atom; C2: secondary carbon atom.

To explore the adsorption mechanism of ethanol molecules on each surface, Mulliken charge population analysis was performed. As shown in Table 2, after the adsorption of ethanol on each surface, the overall charge of ethanol molecules is negative, indicating that electrons are transferred from the surface to the ethanol molecules. When the OC is reduced from Fe_2O_3 to FeO, the amount of charge transferred decreases, which is consistent with the change of C-C bond length, indicating that the adsorption effect gradually decreases. As shown in Figure 4, with the reduction of Fe_2O_3, the absolute value of E_{ads} gradually increases, indicating the reduction of Fe_2O_3 benefits the adsorption process, which corresponds to the previous report [32].

Table 2. Mulliken atomic charge population of the ethanol molecule on each surface.

Atom	Ethanol Molecule	Ethanol Molecule on $Fe_2O_3(001)$	Ethanol Molecule on $Fe_3O_4(001)$	Ethanol Molecule on FeO(001)	Ethanol Molecule on $FeO_{0.375}(001)$
			Charge		
C1	−0.14	−0.73	−0.71	−0.7	−0.65
H1	0.045	0.19	0.19	0.17	0.1
H2	0.06	0.23	0.2	0.18	0.17
H3	0.061	0.25	0.26	0.28	0.25
C2	0.147	−0.28	−0.29	−0.31	−0.28
H4	0.034	0.24	0.26	0.27	0.22
H5	0.036	0.27	0.27	0.28	0.27
O of Hydroxyl	−0.488	−0.76	−0.71	−0.66	−0.61
H of Hydroxyl	0.246	0.51	0.48	0.48	0.44
Net charge	0.001	−0.08	−0.05	−0.01	−0.09

H1, H2, H3: H atoms connected to primary carbon atoms; H4, H5: each H atom is connected to the secondary carbon atoms.

3.2. Ethanol Deep Decomposition on Fe₂O₃(001)

After ethanol molecules are stably adsorbed on the surface of $Fe_2O_3(001)$, they will decompose under the promotion of the OC and produce a series of intermediate products. To study the decomposition mechanism and reaction path of ethanol on $Fe_2O_3(001)$, the stable adsorption of ethanol molecules on $Fe_2O_3(001)$ was set as the initial state (IS). Then, LST/QST was used to search for the transition state of the reaction, and the reaction activation energy (E_a) and reaction energy (E_r) were obtained at the same time.

According to the principle of minimum activation energy (energy barrier), the decomposition reaction path of ethanol molecules on the $Fe_2O_3(001)$ can be obtained, as shown in Figure 5. Among the first step reaction of the decomposition reaction of ethanol molecules on $Fe_2O_3(001)$, the energy barrier of the dehydroxylation reaction of ethanol molecules is the lowest, only 3.302 eV, and the reaction process is exothermic, of which the energy is −0.689 eV. Therefore, the first decomposition reaction step of ethanol molecules is most likely to be a dehydroxylation reaction. This is different from that of the first step of the decomposition reaction of ethanol molecules on the nickel-based OC, the dehydration reaction, which was obtained by Dou et al., using Fourier infrared spectroscopy [31]. The energy barrier of the ethanol dehydration reaction on the $Fe_2O_3(001)$ surface is 7.132 eV, which is higher than the energy barrier of the ethanol dehydroxylation reaction. This may be due to the different characteristics of nickel-based OCs and iron-based OCs. The lowest energy barrier for the second step of the decomposition reaction of ethanol is the breaking process of the C-C bond (called Reaction Path A). The reaction energy barrier is 3.383 eV, and the E_r is 2.756 eV. However, in the second step of decomposition, the cleavage of the C1-H bond of the ethyl group (called Reaction Path B) has a reaction energy barrier of 3.869 eV, and its E_r is 0.809 eV. The process model of the decomposition reaction of ethanol on $Fe_2O_3(001)$ is shown in Figure 6. In Path A, the ethyl group undergoes a C-C bond cleavage to produce a methyl group. However, the generated methyl group is not absorbed on the surface of the OC, and it combines with the free hydrogen atoms generated by dehydrogenation in the other reaction pathways to generate methane. In Path B, the Fe-C bond between the ethyl group and the iron atom on the surface of the OC is broken. At the same time, the C1-H bond of the ethyl group is broken, forming a free ethylene molecule and a H atom, and the H atom is adsorbed on the iron atoms on the surface. Paths A and B, respectively, explain the reaction mechanism of ethanol decomposition to produce methane [13,31–33] and ethylene [34,35].
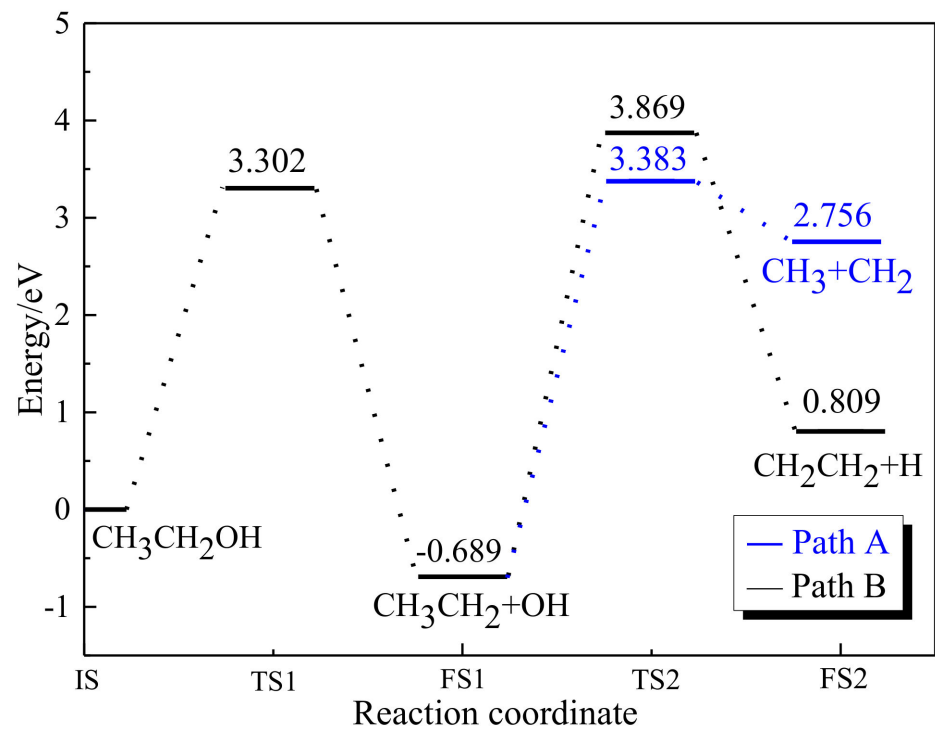
Figure 5. Energy profile for ethanol decomposition on Fe$_2$O$_3$(001) through Reaction Paths A and B.

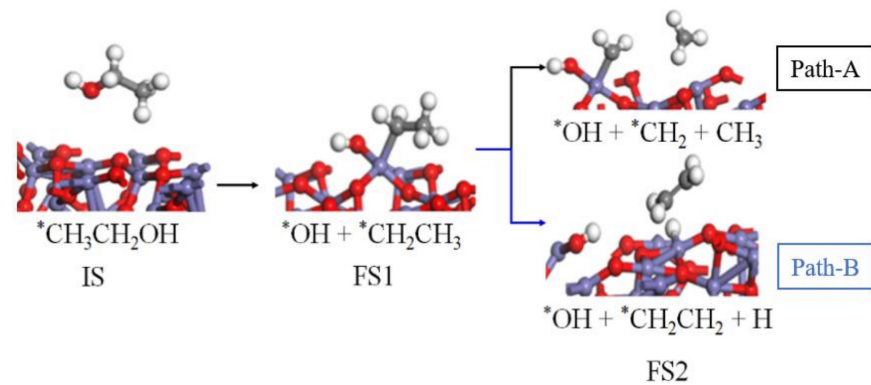**Figure 6.** Configurations for ethanol decomposition on Fe$_2$O$_3$(001) through Reaction Paths A and B (●O, ●Fe, ○H, and ●C. "*" means that the group is adsorbed on the surface of Fe$_2$O$_3$(001)).

3.3. Ethanol Deep Decomposition on Fe$_3$O$_4$(001)

To explore the influence of the OC on the decomposition path of ethanol molecules after the loss of lattice oxygen, the decomposition mechanism and reaction path of ethanol on the surface of Fe$_3$O$_4$(001) were studied. As shown in Figure 7, there are four decomposition reaction paths of ethanol molecules on Fe$_3$O$_4$(001). In the first step of the decomposition reaction, the E_a of the C-C bond cleavage reaction and the O-H bond cleavage reaction is similar, respectively, 3.760 and 3.802 eV, which are lower than others, thus these two decomposition reactions may be the first decomposition reaction step of the ethanol molecules on Fe$_3$O$_4$ (001). In the second step, the O-H bond cleavage reaction of the CH$_2$OH group produced in the first reaction is the lowest energy barrier, only 2.476 eV, and E_r is -0.458 eV (called Reaction Path A). According to the reaction energy barrier diagram, Reaction Path A is the optimal reaction path, and it is an exothermic reaction. Path C is an exothermic reaction as well, and Paths B and D are endothermic reactions that are not easy to react.
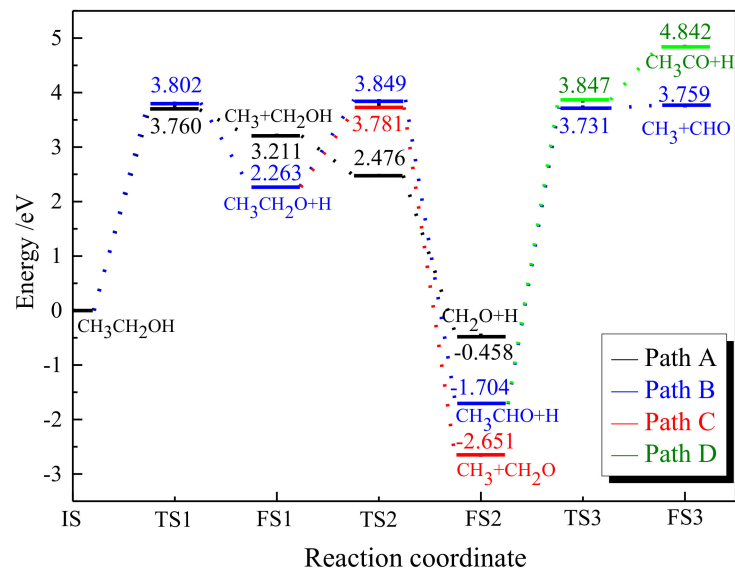
Figure 7. Energy profile for ethanol decomposition on Fe$_3$O$_4$(001) through Reaction Paths A–D.

Decomposition Reaction Paths A–D are shown in Figure 8. In Decomposition Reaction Path A, the product obtained after the cleavage of the C-C bond does not chemically adsorb on Fe$_3$O$_4$(001) to produce chemical bonds. The product methyl group can combine with free hydrogen atoms generated by other reaction pathways to generate methane, which may be a source of methane generated in the ethanol CLG experiment [34,35]. In another product, the CH$_2$OH group, the C-O single bond becomes a C=O double bond, and when the O-H bond is broken, it becomes a formaldehyde molecule. In Decomposition Reaction Path B, the C=O double bond in CH$_3$CHO becomes the C≡O triple bond. The C≡O triple bond is a unique bond type of CO molecules, which may be the formation mechanism of free CO molecules [22,36].
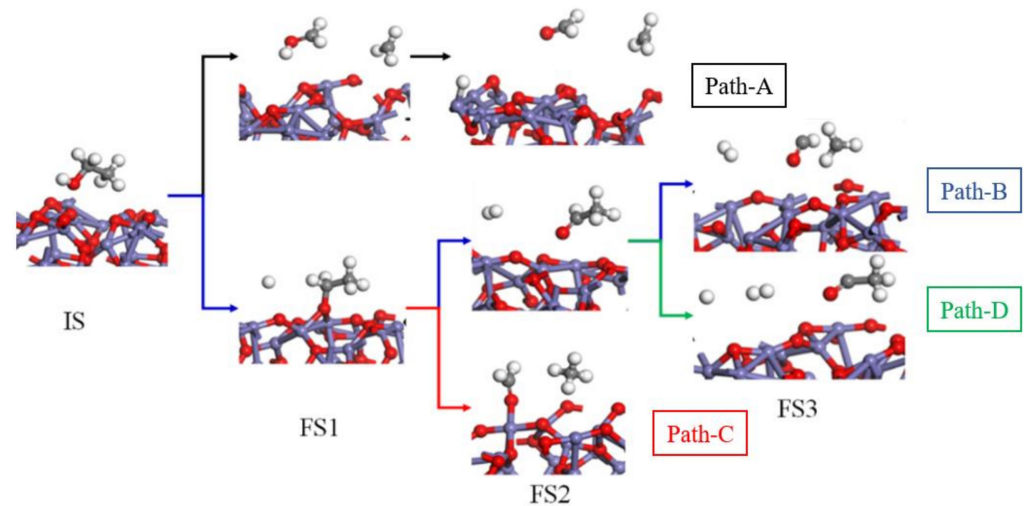

Figure 8. Configurations for ethanol decomposition on Fe$_3$O$_4$(001) through Reaction Paths A–D (●O, ●Fe, ○H, and ●C).

3.4. Ethanol Deep Decomposition FeO(001)

From the perspective of the first decomposition reaction step, compared with Fe$_2$O$_3$(001), the Ea of the dehydrogenation reaction on FeO(001) is greatly decreased, indicating that FeO has a good catalytic effect on the ethanol decomposition reaction. Additionally, the energy barrier for the dehydration reaction of ethanol on FeO(001) is 2.923 eV, which is different from the ethanol decomposition reaction path on NiO described in the literature [31]. As shown in

Figure 9, the energy barrier of Reaction Path A is low, so ethanol molecules are most likely to undergo dehydroxylation on FeO(001) first, and then the C-C bond cleavage reaction occurs.
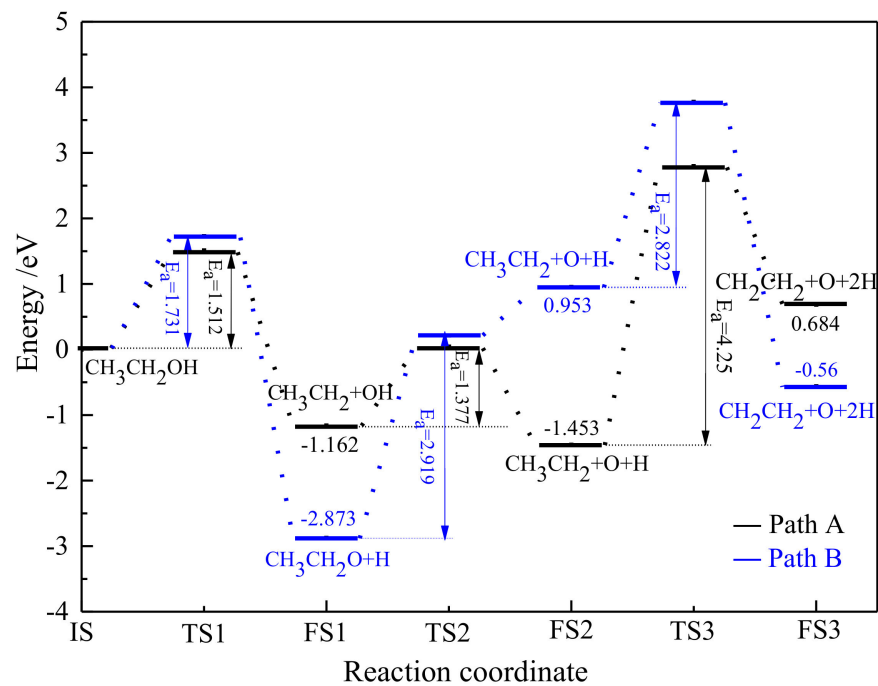

Figure 9. Energy profile for ethanol decomposition on FeO(001) through Reaction Paths A and B.

As shown in Figure 10, in Decomposition Reaction Path A, the ethanol molecules first undergo a dehydroxylation reaction on FeO(001). The detached hydroxyl group is adsorbed on FeO(001), and a free ethyl group is generated. Subsequently, the O-H bond is broken, and the broken H atoms are adsorbed on FeO(001). Finally, the C1-H bond breaks, creating a free ethylene molecule with non-coplanar atoms. In Decomposition Reaction Path B, CH_3CH_2O groups and H atoms are generated by breaking the O-H bond of the ethanol molecules. Then CH_3CH_2O groups are adsorbed on FeO(001), but H atoms are not adsorbed. After the C-O bond in the CH_3CH_2O group is broken, an ethyl group and an O atom are generated immediately. The O atom is adsorbed on the OC surface and becomes part of the OC surface, which reduces the degree of reduction on the OC surface. It reveals the mechanism of ethanol oxidation on the surface of the OC. Finally, the C1-H bond of the ethyl group is broken, producing an ethylene molecule [20].
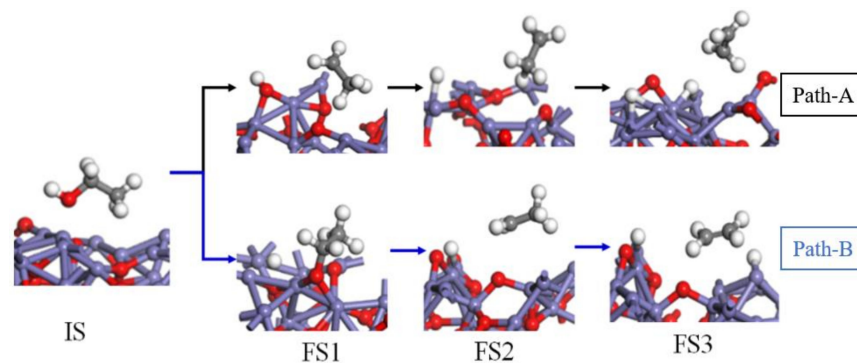

Figure 10. Configurations for ethanol decomposition on FeO(001) through Reaction Paths A and B (●O, ●Fe, ●H, and ●C).

3.5. Ethanol Deep Decomposition on FeO$_{0.375}$(001)

As shown in Figure 11, there are six decomposition reaction paths of ethanol molecules on FeO$_{0.375}$(001). In the first step, the Ea of the dehydroxylation reaction is similar to the Ea of the O-H bond cleavage reaction, which is similar to the decomposition reaction on FeO(001). Therefore, both types of decomposition reactions may be the first decomposition reaction step of ethanol molecules on FeO$_{0.375}$(001). In the second step of Path A, the energy barrier of the C-O bond cleavage reaction of the CH$_3$CH$_2$O group is the lowest, only 1.488 eV, and its Er is 1.202 eV. The C2-H bond cleavage reaction acts as the third step of Path A, with an energy barrier of 0.138 eV, and its Er is −10.716 eV. Thus, among six decomposition reaction paths, Path A is the most feasible reaction pathway.
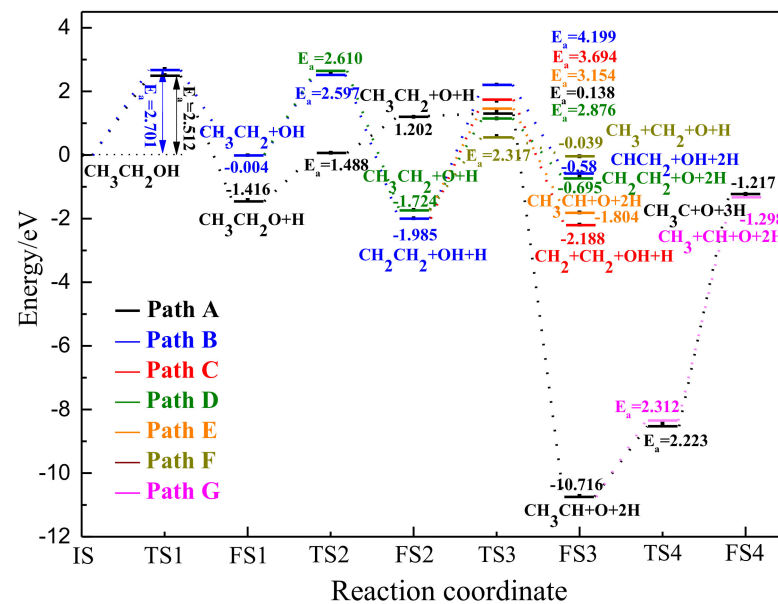

Figure 11. Energy profile for ethanol decomposition on FeO$_{0.375}$(001) through Reaction Paths A–G.

Decomposition Reaction Paths A–F are shown in Figure 12. In Path A, the first decomposition reaction step of the ethanol molecules on the FeO$_{0.375}$(001) surface is the breaking of the O-H bond. Then the hydroxyl O atom is adsorbed on the OC surface. The second step is the breaking of the C-O bond, creating a free CH$_3$CH$_2$ group, and then the C2-H bond is broken, with the H atom and the CH$_3$CH group adsorbed on the same Fe atom on the surface of FeO$_{0.375}$(001). Finally, the C2-H bond broke again, and the Fe-C bond becomes the Fe-C-Fe bond. The formation of this bond may cause carbon deposition [10,37]. The broken H atom is adsorbed on FeO$_{0.375}$(001) to form the Fe-H-Fe bond, and the previously adsorbed H atom also forms the Fe-H-Fe bond, which may indicate that the highly reduced OC FeO$_{0.375}$(001) surface is not conducive to the formation of free H atoms, thereby inhibiting the decomposition of ethanol to produce H$_2$.
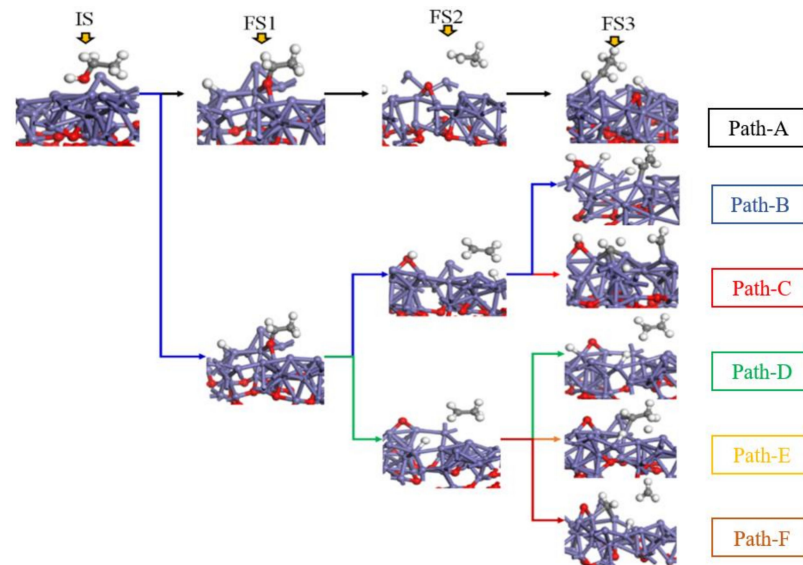
Figure 12. Configurations for ethanol decomposition on $FeO_{0.375}(001)$ through Reaction Paths A–F (●O, ●Fe, ○H, and ●C).

3.6. Thermodynamic Analysis

Since Fe only has a catalytic effect on the decomposition of ethanol molecules and does not directly participate in the chain reaction, and only Fe_2O_3, Fe_3O_4, and FeO can take part in the oxidation of ethanol during the CLG process, the reduction of the OC will follow a decreasing of oxygen potential as $Fe_2O_3 \rightarrow Fe_3O_4 \rightarrow FeO \rightarrow Fe$. We compared two CLG cases following the carbon conversion to CO and $CO_2 + CH_4$, respectively. The possible reactions are concluded as follows:
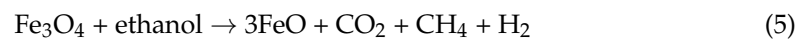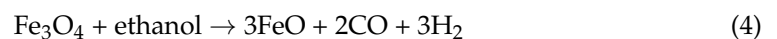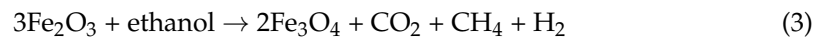
$$3Fe_2O_3 + ethanol \rightarrow 2Fe_3O_4 + 2CO + 3H_2 \tag{2}$$

$$3Fe_2O_3 + ethanol \rightarrow 2Fe_3O_4 + CO_2 + CH_4 + H_2 \tag{3}$$

$$Fe_3O_4 + ethanol \rightarrow 3FeO + 2CO + 3H_2 \tag{4}$$

$$Fe_3O_4 + ethanol \rightarrow 3FeO + CO_2 + CH_4 + H_2 \tag{5}$$

$$FeO + ethanol \rightarrow Fe + 2CO + 3H_2 \tag{6}$$

$$FeO + ethanol \rightarrow Fe + CO_2 + CH_4 + H_2 \tag{7}$$

Figure 13 compares the free energy change (ΔG) and reaction enthalpy change (ΔH) for Reactions (2)–(7) under different reaction temperatures. All ΔG is negative, and the reaction can occur spontaneously. The reaction that only produces CO and H_2 is more likely to occur with the increase of reaction temperature [38], which is similar to the previous experiment results [20], while ΔG for the reaction leads to CO_2, and CH_4 generation does not change significantly with temperature. Comparing with the decomposition mechanism discussed above, we observed that the reaction of forming CO and H_2 is easier to proceed than that of forming CO_2 and CH_4, which corresponds to the previous report that it is more possible to cross the energy barrier to form H_2 [39]. From the analysis of the reaction mechanism, the reaction energy barrier of the ethanol molecule on FeO is the lowest and more active for catalytic decomposition of ethanol to produce hydrogen than other reduced surfaces, which is similar to the previous result where FeO possesses superior catalytic hydrogen production capabilities [40]. For Figure 13a,c, the reaction enthalpy appeared to decrease first and then increase, which suggests that these reactions are controlled by both thermodynamics and kinetic. Since these reactions are all exothermic reactions, low temperature is conducive to the reaction equilibrium, but the reaction requires a certain high temperature to cross the reaction energy barrier. Therefore, based

on reaction thermodynamics and kinetics, there is an optimal reaction temperature. In our previous experiment, 900 °C is the optimal reaction temperature of ethanol CLG [20], which corresponds to the previously reported experimental results [38]. In addition, the feasibility of Fe_2O_3 material used as OC in the CLG is demonstrated [41], good cycle performance of an iron-based OC been proven [42], the energy balance of ethanol CLG has been discussed [20], and the significant long-term efficiency potential of the chemical looping combustion (CLC)-based coal-fired power plant system [43], as well as the economic feasibility of the CLC-steam methane-reforming (SMR) system [44], have been revealed. However, after circulation, the accumulation of char will reduce the H_2 production in CLG [45]. It is necessary to determine the optimal reaction pressure [46] and structure of the OC [47,48] to improve the circulation of OC in the CLG process.
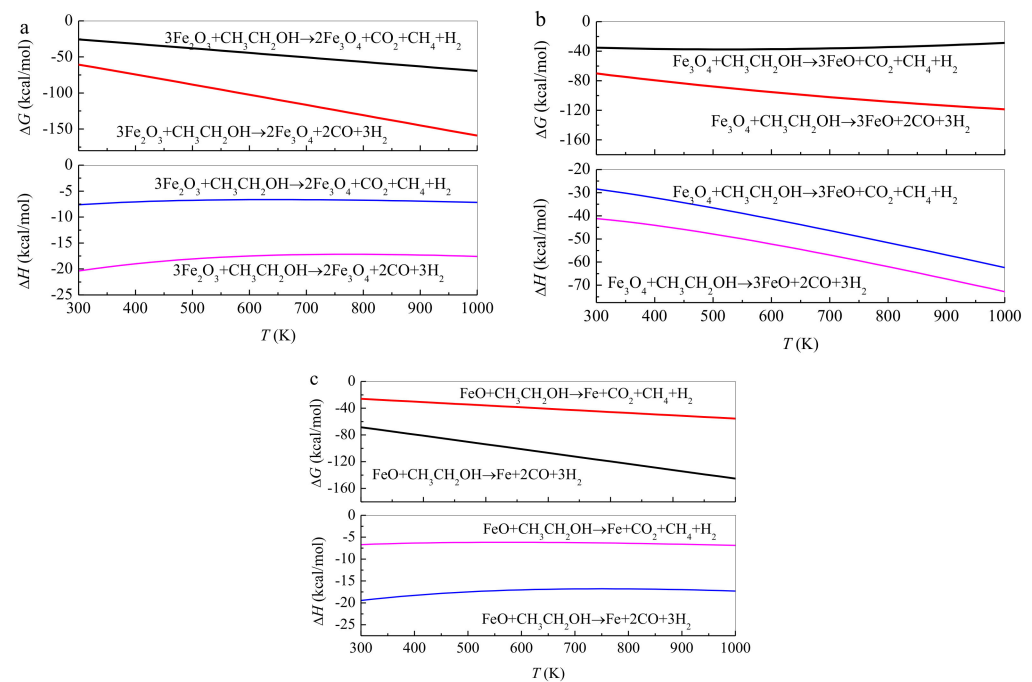

Figure 13. Reaction free energy (ΔG) and reaction enthalpy (ΔH) from Reactions (2)–(7) under different reaction temperatures. (Ethanol decomposes on Fe_2O_3 (**a**), Fe_3O_4 (**b**) and FeO (**c**) respectively).

4. Conclusions

This paper used periodic DFT to study the adsorption and decomposition reaction mechanism of ethanol molecules on Fe_2O_3(001) and its reduced surfaces. The results show that in the CLG process, ethanol molecules are physically adsorbed on Fe_2O_3(001) and its reduced surfaces, which are all exothermic processes. As Fe_2O_3 loses the lattice oxygen, the net charge obtained by the ethanol molecules first increases and then decreases. As lattice oxygen continues to decrease, the energy barrier of the decomposition reaction of ethanol on the reduced Fe_2O_3 increases first, decreases, and then increases. The decomposition reaction energy barrier of the ethanol molecules on FeO(001) is the lowest and more active for catalytic decomposition of ethanol than other reduced surfaces. The results of the thermodynamic analysis show that ethanol molecules are more likely to produce hydrogen on FeO, which is consistent with the results of the kinetic analysis.

Author Contributions: Conceptualization, W.Q. and L.L.; Methodology, W.Q.; Resources, W.Q.; Software, L.L., X.Z. and J.W.; Formal analysis, L.L. and X.Z.; Supervision, X.X.; Funding acquisition, X.X.; Writing—original draft, L.L.; Writing—review & editing, Z.Z., L.L. and X.X. All authors have read and agreed to the published version of the manuscript.

Institutional Review Board Statement: Not applicable.

Informed Consent Statement: Not applicable.

Data Availability Statement: The data presented in this study are available on request from the corresponding author.

Conflicts of Interest: The authors declare no conflict of interest.

References

1. Yu, Z.; Li, C.; Jing, X.; Zhang, Q.; Wang, Z.; Fang, Y.; Huang, J. Catalytic chemical looping combustion of carbon with an iron-based oxygen carrier modified by K_2CO_3: Catalytic mechanism and multicycle tests. *Fuel Process. Technol.* **2015**, *135*, 119–124. [CrossRef]
2. Singh, L.; Wahid, Z.A. Methods for enhancing bio-hydrogen production from biological process: A review. *J. Ind. Eng. Chem.* **2015**, *21*, 70–80. [CrossRef]
3. Kang, D.; Lim, H.S.; Lee, M.; Lee, J.W. Syngas production on a Ni-enhanced Fe_2O_3/Al_2O_3 oxygen carrier via chemical looping partial oxidation with dry reforming of methane. *Appl. Energy* **2018**, *211*, 174–186. [CrossRef]
4. Liu, G.; Liao, Y.; Wu, Y.; Ma, X.; Chen, L. Characteristics of microalgae gasification through chemical looping in the presence of steam. *Int. J. Hydrogen Energy* **2017**, *42*, 22730–22742. [CrossRef]
5. Zeng, J.; Xiao, R.; Zhang, H.; Wang, Y.; Zeng, D.; Ma, Z. Chemical looping pyrolysis-gasification of biomass for high H_2/CO syngas production. *Fuel Process. Technol.* **2017**, *168*, 116–122. [CrossRef]
6. Nandy, A.; Loha, C.; Gu, S.; Sarkar, P.; Karmakar, M.K.; Chatterjee, P.K. Present status and overview of chemical looping combustion technology. *Renew. Sust. Energy Rev.* **2016**, *59*, 597–619. [CrossRef]
7. Yuan, Y.; Dong, X.; Ricardez-Sandoval, L. A density functional theory analysis on syngas adsorption on NiO (100) surface. *Appl. Surf. Sci.* **2019**, *498*, 143782. [CrossRef]
8. Huang, Z.; He, F.; Zhao, K.; Zheng, A.Q.; Li, H.B.; Zhao, Z.L. Synthesis gas production by chemical-looping reforming of methane using lattice oxygen. *Prog. Chem.* **2012**, *24*, 1599–1609.
9. Yuan, Y.; Dong, X.; Ricardez-Sandoval, L. A multi-scale simulation of syngas combustion reactions by Ni-based oxygen carriers for chemical looping combustion. *Appl. Surf. Sci.* **2020**, *531*, 147277. [CrossRef]
10. Chen, L.; Kong, L.; Bao, J.; Combs, M.; Nikolic, H.S.; Fan, Z.; Liu, K. Experimental evaluations of solid-fueled pressurized chemical looping combustion—The effects of pressure, solid fuel and iron-based oxygen carriers. *Appl. Energy* **2017**, *195*, 1012–1022. [CrossRef]
11. Liu, H.; Chen, T.; Chang, D.; Chen, D.; He, H.; Frost, R.L. Catalytic cracking of tar derived from rice hull gasification over palygorskite-supported Fe and Ni. *J. Mol. Catal. A Chem.* **2012**, *363*, 304–310. [CrossRef]
12. Wang, W.; Fan, L.; Wang, G. Study on chemical looping reforming of ethanol (CLRE) for hydrogen production using $NiMn_2O_4$ spinel as oxygen carrier. *J. Energy Inst.* **2017**, *90*, 884–892. [CrossRef]
13. Huang, Z.; Zhang, Y.; Fu, J.; Yu, L.; Chen, M.; Liu, S.; He, F.; Chen, D.; Wei, G.; Zhao, K.; et al. Chemical looping gasification of biomass char using iron ore as an oxygen carrier. *Int. J. Hydrogen Energy* **2016**, *41*, 17871–17883. [CrossRef]
14. Zeng, J.; Xiao, R.; Zeng, D.; Zhao, Y.; Zhang, H.; Shen, D. High H_2/CO ratio syngas production from chemical looping gasification ofsawdust in a dual fluidized bed gasifier. *Energy Fuels* **2015**, *30*, 1764–1770. [CrossRef]
15. Wei, G.; He, F.; Zhao, Z.; Huang, Z.; Zheng, A.; Zhao, K.; Li, H. Performance of Fe–Ni bimetallic oxygen carriers for chemical looping gasification of biomass in a 10 kWth interconnected circulating fluidized bed reactor. *Int. J. Hydrogen Energy* **2015**, *40*, 16021–16032. [CrossRef]
16. Qin, W.; Wang, Y.; Dong, C.; Zhang, J.; Chen, Q.; Yang, Y. The synergetic effect of metal oxide support on Fe_2O_3 for chemical looping combustion: A theoretical study. *Appl. Surf. Sci.* **2013**, *282*, 718–723. [CrossRef]
17. Feng, Y.; Wang, N.; Guo, X.; Zhang, S. Reaction mechanism of $Ca_2Fe_2O_5$ oxygen carrier with CO in chemical looping hydrogen production. *Appl. Surf. Sci.* **2020**, *534*, 147583. [CrossRef]
18. Qin, W.; Chen, Q.; Wang, Y.; Dong, C.; Zhang, J.; Li, W.; Yang, Y. Theoretical study of oxidation–reduction reaction of Fe_2O_3 supported on MgO during chemical looping combustion. *Appl. Surf. Sci.* **2013**, *266*, 350–354. [CrossRef]
19. Qin, W.; Chen, S.; Zhu, J.; Zhang, M.; Xiao, X. Hydrogen production by chemical looping gasification of corn stalk driven by a tert-butanol solution. *Chem. Res. Chin. Univ.* **2019**, *35*, 1012–1017. [CrossRef]
20. Qin, W.; Wang, J.; Luo, L.; Liu, L.; Xiao, X.; Zheng, Z.; Sun, S.; Hu, X.; Dong, C. Chemical looping reforming of ethanol-containing organic wastewater for high ratio H_2/CO syngas with iron-based oxygen carrier. *Int. J. Hydrogen Energy* **2018**, *43*, 12985–12998. [CrossRef]

21. Qin, W.; Chen, S.; Ma, B.; Wang, J.; Li, J.; Liang, R.; Xu, Z.; Liu, L.; Dong, C.; Zhang, H. Methanol solution promoting cotton fiber chemical looping gasification for high H_2/CO ratio syngas. *Int. J. Hydrogen Energy* **2019**, *44*, 7149–7157. [CrossRef]
22. Dou, B.; Zhang, H.; Cui, G.; Wang, Z.; Jiang, B.; Wang, K.; Chen, H.; Xu, Y. Hydrogen production and reduction of Ni-based oxygen carriers during chemical looping steam reforming of ethanol in a fixed-bed reactor. *Int. J. Hydrogen Energy* **2017**, *42*, 26217–26230. [CrossRef]
23. Jiang, B.; Dou, B.; Wang, K. Hydrogen production by chemical looping steam reforming of ethanol using NiO/montmorillonite oxygen carriers in a fixed-bed reactor. *Chem. Eng. J.* **2016**, *298*, 96–106. [CrossRef]
24. García-Labiano, F.; García-Díez, E.; de Diego, L.F.; Serrano, A.; Abad, A.; Gayán, P.; Adánez, J.; Ruíz, J.A.C. Syngas/H_2 production from bioethanol in a continuous chemical-looping reforming prototype. *Fuel Process. Technol.* **2015**, *137*, 24–30. [CrossRef]
25. Adanez, J.; Abad, A.; Garcia-Labiano, F.; Gayan, P.; de Diego, L.F. Progress in Chemical-Looping Combustion and Reforming technologies. *Prog. Energ. Combust.* **2012**, *38*, 215–282. [CrossRef]
26. Dong, C.; Sheng, S.; Qin, W.; Lu, Q.; Zhao, Y.; Wang, X.; Zhang, J. Density functional theory study on activity of α-Fe_2O_3 in chemical-looping combustion system. *Appl. Surf. Sci.* **2011**, *257*, 8647–8652. [CrossRef]
27. Lin, C.; Qin, W.; Dong, C. H_2S adsorption and decomposition on the gradually reduced α-Fe_2O_3(001) surface: A DFT study. *Appl. Surf. Sci.* **2016**, *387*, 720–731. [CrossRef]
28. Xiao, X.; Qin, W.; Wang, J.; Li, J.; Dong, C. Effect of surface Fe-S hybrid structure on the activity of the perfect and reduced α-Fe_2O_3(001) for chemical looping combustion. *Appl. Surf. Sci.* **2018**, *440*, 29–34. [CrossRef]
29. Zhang, Q.; Li, L.; Jiang, B. An intelligent oxygen carrier of $La_{2-x}Sr_xNiO_{4-\lambda}$ for hydrogen production by chemical looping reforming of ethanol. *Int. J. Hydrogen Energy* **2017**, *42*, 17102–17111. [CrossRef]
30. Dou, B.; Wang, C.; Song, Y.; Chen, H.; Jiang, B.; Yang, M.; Xu, Y. Solid sorbents for in-situ CO_2 removal during sorption-enhanced steam reforming process: A review. *Renew. Sust. Energ. Rev.* **2016**, *53*, 536–546. [CrossRef]
31. Zhang, G.; Cui, G.; Dou, B.; Wang, Z.; Goula, M.A. An experimental investigation of forced convection heat transfer with novel microencapsulated phase change material slurries in a circular tube under constant heat flux. *Energy Convers. Manag.* **2018**, *171*, 699–709. [CrossRef]
32. Lin, C.; Qin, W.; Dong, C. Reduction effect of α-Fe_2O_3 on carbon deposition and CO oxidation during chemical-looping combustion. *Chem. Eng. J.* **2016**, *301*, 257–265. [CrossRef]
33. Bayham, S.C.; Kim, H.R.; Wang, D.; Tong, A.; Zeng, L.; McGiveron, O.; Kathe, M.V.; Chung, E.; Wang, W.; Wang, A.; et al. Iron-based coal direct chemical looping combustion process: 200-h continuous operation of a 25-kWth subpilot unit. *Energy Fuels* **2013**, *27*, 1347–1356. [CrossRef]
34. Chein, R.; Hsu, W. Thermodynamic equilibrium analysis of H_2-rich syngas production via sorption-enhanced chemical looping biomass gasification. *Renew. Energy* **2020**, *153*, 117–129. [CrossRef]
35. Yan, J.; Sun, R.; Shen, L.; Bai, H.; Jiang, S.; Xiao, Y.; Song, T. Hydrogen-rich syngas production with tar elimination via biomass chemical looping gasification (BCLG) using $BaFe_2O_4$/Al_2O_3 as oxygen carrier. *Chem. Eng. J.* **2020**, *387*, 124107. [CrossRef]
36. Zaini, I.N.; Nurdiawati, A.; Aziz, M. Cogeneration of power and H_2 by steam gasification and syngas chemical looping of macroalgae. *Appl. Energy* **2017**, *207*, 134–145. [CrossRef]
37. Sarafraz, M.M.; Jafarian, M.; Arjomandi, M.; Nathan, G.J. Potential use of liquid metal oxides for chemical looping gasification: A thermodynamic assessment. *Appl. Energy* **2017**, *195*, 702–712. [CrossRef]
38. Hu, Z.; Jiang, E.; Ma, X. The effect of oxygen carrier content and temperature on chemical looping gasification of microalgae for syngas production. *J. Energy. Inst.* **2019**, *92*, 474–487. [CrossRef]
39. Huang, Z.; Liu, S.; Li, D.; Zhan, Z.; He, F.; Li, H. Study on thermodynamic simulation of biomass chemical chain gasification based on Fe_2O_3 oxygen carrier. *Act. Energ. Sol. Sin.* **2017**, *5*, 1421–1430.
40. Kment, S.; Sivula, K.; Naldoni, A.; Sarmah, S.P.; Kmentová, H.; Kulkarni, M.; Rambabu, Y.; Schmuki, P.; Zbořil, R. FeO-based nanostructures and nanohybrids for photoelectrochemical water splitting. *Prog. Mater. Sci.* **2020**, *110*, 100632. [CrossRef]
41. Huang, Z.; He, F.; Zhu, H.; Chen, D.; Zhao, K.; Wei, G.; Feng, Y.; Zheng, A.; Zhao, Z.; Li, H. Thermodynamic analysis and thermogravimetric investigation on chemical looping gasification of biomass char under different atmospheres with Fe_2O_3 oxygen carrier. *Appl. Energy* **2015**, *157*, 546–553. [CrossRef]
42. Qin, W.; Wang, Y.; Lin, C.; Hu, X.; Dong, C. Possibility of morphological control to improve the activity of oxygen carriers for chemical looping combustion. *Energy Fuels* **2015**, *29*, 1210–1218. [CrossRef]
43. Zou, X.; Zhao, H.; Zheng, C. Techno-economic evaluation of chemical looping-based coal-fired power plant. *Proc. CSEE* **2014**, *35*, 34–43.
44. Fan, J.; Zhu, L.; Jiang, P.; Li, L.; Liu, H. Comparative exergy analysis of chemical looping combustion thermally coupled and conventional steam methane reforming for hydrogen production. *J. Clean. Prod.* **2016**, *131*, 247–258. [CrossRef]
45. Hu, Q.; Shen, Y.; Chew, J.W.; Ge, T.; Wang, C. Chemical looping gasification of biomass with Fe_2O_3/CaO as the oxygen carrier for hydrogen-enriched syngas production. *Chem. Eng. J.* **2020**, *379*, 122346. [CrossRef]
46. Chen, H.; Zhao, C.; Li, Y.; Chen, X. CO_2 capture performance of calcium-based sorbents in a pressurized carbonation/calcination loop. *Energy Fuels* **2010**, *24*, 5751–5756. [CrossRef]

47. Li, Y.; Su, M.; Xie, X.; Wu, S.; Liu, C. CO_2 capture performance of synthetic sorbent prepared from carbide slag and aluminum nitrate hydrate by combustion synthesis. *Appl. Energy* **2015**, *145*, 60–68. [CrossRef]
48. Ma, X.; Li, Y.; Yan, X.; Zhang, W.; Zhao, J.; Wang, Z. Preparation of a morph-genetic CaO-based sorbent using paper fibre as a biotemplate for enhanced CO_2 capture. *Chem. Eng. J.* **2019**, *361*, 235–244. [CrossRef]